J. Fluid Mech. (2023), *vol.* 975, A21, doi:10.1017/jfm.2023.827

Strong coupling of flow structure and heat transport in liquid metal thermal convection

Xin-Yuan Chen[1], **Yi-Chao Xie**[1], **Juan-Cheng Yang**[1,†] **and Ming-Jiu Ni**[1,2,†]

[1]State Key Laboratory for Strength and Vibration of Mechanical Structures, School of Aerospace, Xi'an Jiaotong University, Xi'an 710049, PR China

[2]School of Engineering Science, University of Chinese Academy of Sciences, Beijing 101408, PR China

(Received 23 January 2023; revised 27 August 2023; accepted 1 October 2023)

A typical feature of thermal convection is the formation of large-scale flow (LSF) structures of the order of system size. How this structure affects global heat transport is an important issue in the study of thermal convection. We present an experimental study of the coupling between the flow structure and heat transport in liquid metal convection with different degrees of spatial confinement, characterized by the aspect ratio Γ of the convection cell. Combining measurements in two convection cells with $\Gamma = 1.0$ and 0.5, the study shows that a large-scale circulation (LSC) transports ∼35 % more heat than a twisted LSC. It is further found that when the LSF is in the form of the LSC state, the system is in a fully developed turbulence state with a $Nu \sim Ra^{0.29}$ scaling for the heat transport. However, the twisted LSC state with a heat transport scaling of $Nu \sim Ra^{0.37}$ appears when the system is not in the fully developed turbulence state. Bistability is observed when the system evolves from the twisted-LSC-dominated to the LSC-dominated state.

Key words: Bénard convection

1. Introduction

Liquid metal thermal convection is ubiquitous in nature and industrial applications. Common examples are the convection in the Earth's outer core (Elsasser 1956; King & Aurnou 2013) and in nuclear fusion reactors (Salavy *et al.* 2007). The ideal model to study thermal convection in the laboratory is the classical Rayleigh–Bénard convection (RBC) system, i.e. a fluid layer in a closed cell cooled from the top plate and heated from the bottom plate (Ahlers, Grossmann & Lohse 2009; Lohse & Xia 2010; Xia 2013) which serves as a paradigmatic model for studying convective turbulence in general. The convection flow is controlled by two dimensionless parameters, the Rayleigh number, $Ra = \alpha g \Delta T H^3/(\nu\kappa)$ representing the ability of thermal driving, and the Prandtl number,

† Email addresses for correspondence: yangjc@xjtu.edu.cn, mjni@ucas.ac.cn

$Pr = \nu/\kappa$. Here α, ν and κ are the thermal expansion coefficient, the kinematic viscosity and thermal diffusivity of the working fluid, respectively; ΔT is the temperature difference between the two plates and g is the gravitational acceleration constant. For liquid metal, due to the thermal diffusivity being much larger than the kinematic viscosity, the Prandtl number is of the order of 10^{-2}. The aspect ratio $\Gamma = D/H$ serves as another control parameter representing the effect of the spatial confinement. Here D and H are the width and height of the cell, respectively. The system response parameter, the Nusselt number, $Nu = qH/(\lambda \Delta T)$, quantifies the heat transport efficiency, where q is the input heat-flux density at the bottom plate and λ is the thermal conductivity of the working fluid.

The discovery of coherent structures is a hallmark of modern turbulence research. Recent studies suggest that the coherent large-scale structures in turbulence may possess different flow states characterized by different topologies (Ravelet *et al.* 2004; de la Torre & Burguete 2007; Cortet *et al.* 2010; Zimmerman, Triana & Lathrop 2011; Huisman *et al.* 2014; Faranda *et al.* 2017; de Wit, van Kan & Alexakis 2022). For example, the momentum transport in turbulent Taylor–Couette flow relies on the number of Taylor vortices (Huisman *et al.* 2014). The transition from convection rolls to a finger structure in double-diffusive convection enhances salinity transport (Yang *et al.* 2020). For rotating Rayleigh–Bénard convection (RRBC), the existence of long-lived Taylor columns tends to carry a large portion of the heat and mass fluxes (Grooms *et al.* 2010). In inclined turbulent thermal convection, the twisting and sloshing oscillations of LSC at a small inclination angle affect the heat transport up to 40 % (Zwirner *et al.* 2020*a*). A distinct feature in RBC is the formation of the large-scale circulation (LSC). It has been shown that the LSC structure depends strongly on the degree of spatial confinement characterized by the aspect ratio Γ, e.g. for $\Gamma > 1$, the side-by-side convection rolls emerge (Wang *et al.* 2020), while for $\Gamma < 1$, the LSC will be divided into several vertically stacked rolls (Verzicco & Camussi 2003; Xi & Xia 2008; Zwirner, Tilgner & Shishkina 2020*b*). For fluids with the Prandtl number $Pr \geq 1$, the difference in heat transfer in cells with different Γ is at most $\sim$5 % (Sun, Xi & Xia 2005; Xi & Xia 2008; Weiss & Ahlers 2011; Xie, Ding & Xia 2018). How this change of flow topology induced by the spatial confinement, i.e. $\Gamma < 1$, in low-*Pr* convection relevant to astrophysical and geophysical applications, alters the heat transport is not yet fully established (Aurnou & Olson 2001; Yanagisawa *et al.* 2010, 2011; Zwirner *et al.* 2020*b*; Yang, Vogt & Eckert 2021; Schindler *et al.* 2022).

In this paper, using Rayleigh–Bénard convection in liquid metal as a model system, combining measurements in two convection cells with $\Gamma = 1.0$ and 0.5, we show that the large-scale flow (LSF) evolves from a twisted large-scale circulation (twisted LSC) state to a normal planar LSC state with increasing of the Rayleigh number *Ra*. The heat transport scaling of the former is $Nu \sim Ra^{0.37}$ and that for the latter is $Nu \sim Ra^{0.29}$. It is further found that when the LSF is in the form of the planar LSC, the system is in a fully developed turbulence state. However, the twisted LSC appears when the system is not in a fully developed turbulence state. The study shows that the LSC transports $\sim$35 % more heat than the twisted LSC when they coexist. The system exhibits bistability in an *Ra* range of $7.30 \times 10^5 \leq Ra \leq 1.62 \times 10^6$.

2. Experimental set-up and measurement methods

The experiment was carried out in cuboid Rayleigh–Bénard convection set-ups. Two convection cells with the aspect ratios of $\Gamma = D/H \approx 1$ and $\Gamma \approx 0.5$ were used. The width D and length L of the cells were $D = L = 5.0$ cm and their heights were $H = 5.3$ cm for $\Gamma \approx 1$ and $H = 10.3$ cm for $\Gamma \approx 0.5$. Each convection cell consists of three parts, i.e.

a top cooling plate, a Plexiglas sidewall and a bottom heating plate. The cooling plate, the heating plate and the Plexiglas sidewall were held together through four nylon rods. The bottom plate with a thickness of 2.5 cm was heated by a resistance wire with its resistance being $R = 9.3\Omega$ at room temperature (OMEGA NI80-015-200). It was buried in straight grooves with a width of 0.2 cm and a depth of 0.4 cm on the backside of the plate. The resistance wire covers an area of $6.0 \times 6.0\ \text{cm}^2$. It was connected to a programmable DC power supply (GWINSTEK PSW 250-13.5) which provides a maximum power of 1080 W. The voltage U supplied to the wire and its current I were measured using a digital multimeter, from which we calculated the input heat flux $q = UI/(DL)$. The top plate with a thickness of 4.0 cm was cooled by circulating temperature-controlled cooling water through two symmetrical channels with a width of 0.6 cm and a depth of 2.6 cm machined on its backside. The channels are connected to a temperature-regulated water tank (XIATECH C3150A) with the temperature control accuracy being 0.01 °C. Both plates were electroplated with a thin layer of nickel to prevent the corrosion of copper by a liquid gallium-indium-tin (GaInSn) alloy.

The temperature boundary condition at the plates needs special discussion. The isothermality of the boundary condition at the plate is characterized by the Biot number, i.e. $Bi = Nu(\lambda/\lambda_{Cu})(H_{Cu}/H)$, where λ and λ_{Cu} are the thermal conductivity of the working fluid and copper, respectively. Here H and H_{Cu} are the thickness of the fluid layer and the copper plate, respectively. In the present experiment, the Biot number varies in the range of $0.037 \le Bi \le 0.152$ for the cell with $\Gamma = 0.5$ and $0.08 \le Bi \le 0.135$ for the cell with $\Gamma = 1$. It is seen that Bi in both cells are smaller than 1. For example, they are of the same order as the previous experimental studies (Aurnou *et al.* 2018; Schindler *et al.* 2022; Xu, Horn & Aurnou 2022), suggesting that the temperature boundary condition at the plate can be treated as an isothermal boundary condition to a good approximation.

The cell is wrapped with thermal insulation material with a thickness of ∼3 cm. To reduce the heat loss, the convection cell is placed in a heating basin which covers the bottom heating plate. The temperature of the basin is controlled in such a way that its temperature equals to that of the bottom plate to reduce heat leakage. In addition, the whole apparatus is placed inside a thermostat. The temperature of the thermostat is set at 35 ± 0.5 °C which is the same as the mean temperature of the fluid. With this set-up, the heat loss has been minimized.

Liquid metal GaInSn was used as the working fluid. The main difference between GaInSn and the most widely studied liquid, that is water, lies in the Prandtl number. At a mean temperature of 35 °C, the corresponding $Pr = 0.029$ for GaInSn compared with $Pr \sim 4.87$ for water at 35 °C, and the viscous boundary layer (BL) is thinner than the thermal BL in the low-Pr fluid. The thermal physical properties of GaInSn used in this experiment are adopted from Plevachuk *et al.* (2014). The Rayleigh number varies in the range of $8.51 \times 10^4 \le Ra \le 5.14 \times 10^5$ for the $\Gamma = 1$ cell and $3.11 \times 10^5 \le Ra \le 7.89 \times 10^6$ for the $\Gamma = 0.5$ cell. Except for the 10-day measurement, each experimental run lasted for 10 000 free-fall times $\tau_{ff} = \sqrt{H/(g\alpha\Delta T)}$ to obtain sufficient statistics.

Local temperatures were measured by 32 thermistors with a sampling rate of 0.47 Hz. To obtain the temperature of the top cooling plate T_t and bottom heating plate T_b, four thermistors were embedded into each plate at 2.0 mm distance away from the copper surface facing the liquid metal and distributed on a circle with a diameter of $D/2$. Its centre was overlapped with that of the top plate. The temperature difference $\Delta T = \langle\overline{T_b}\rangle - \langle\overline{T_t}\rangle$ was calculated based on the measured T_t and T_b, from which we obtain Ra and Nu. Here $\langle\cdots\rangle$ represents time averaging and $\overline{\cdots}$ represents spatial averaging. The temperature deviation from the mean plate temperature, i.e. $\langle(T_{k,i} - \langle\overline{T_k}\rangle)/\Delta T\rangle$,

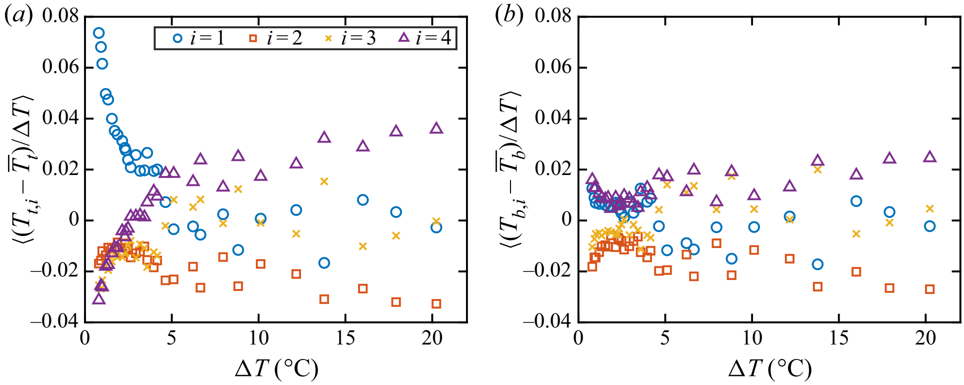

Figure 1. Time-averaged normalized temperature deviation from the mean temperature of individual plates as a function of ΔT for the (*a*) top and (*b*) bottom plates. The subscripts t and b denote the top and bottom plates, respectively. The numbers 1–4 correspond to the four thermistors inside each plate.

where $k = t, b$ represents the top and bottom plate, respectively, and $i = 1, 2, 3, 4$ represents four thermistors in the plate, is shown in figure 1. It is seen that the temperature deviation from the mean is within $\pm 4\,\%$ of the applied temperature difference ΔT except for one thermistor located at the inlet/outlet of the cooling water connector. In addition, the temperature at the cell centre was measured by a thermistor with a head diameter of 380 μm at a sampling rate of 20 Hz.

A multi-thermal-probe method was used to measure the dynamics of the LSF, which has been shown to be capable of measuring the dynamics of the LSC in different cell geometry and varying Pr numbers (Cioni, Ciliberto & Sommeria 1997; Brown & Ahlers 2009; Xie, Wei & Xia 2013; Ren *et al.* 2022). To do so, 24 thermistors were placed inside small blind holes drilled into the sidewall to measure the spatial distribution of the temperatures at three heights, i.e. at $z = 3H/4$, $H/2$ and $H/4$ from the bottom plate. At each z, eight thermistors were equally spaced along the azimuth. The temperature profile at each height was fitted by $T_i = T_0 + A\cos(i\pi/4 - \theta)$ $(i = 0 \ldots 7)$ with T_0 being the mean temperature of the eight thermistors. At each time step, we obtained the flow strength A and the azimuthal orientation θ of the LSF. Here θ is defined as the azimuthal position where the hot fluid ascends. The strength and azimuthal orientations of the LSF at three heights are denoted as A_t, A_m and A_b, and θ_t, θ_m and θ_b for the top, middle and bottom heights, respectively.

The LSF velocity is measured by the ultrasonic Doppler velocimetery (UDV), which contains four ultrasonic transducers with a pulse emission frequency of 8 MHz. They were mounted on two orthogonal sides of the sidewall to measure the velocity in two orthogonal directions at two heights with a sampling rate of 2 Hz. See figure 3(*e*) for an illustration of the distribution of the UDV transducers. At each height, the two ultrasonic beams crossed each other. In such a way, the two-dimensional velocity near the top v_t and that near the bottom plate v_b, i.e. point A and point B in figure 3(*e*), can be obtained. The velocity of the LSF is calculated by the average of the velocity near the top and bottom plates, i.e. $v_{LSF} = (v_t + v_b)/2$.

3. Results and discussions

3.1. *Bistability of the large-scale flow*

Figure 2(*a*) shows a segment of the 10-day time series of Nu measured at $Ra = 1.20 \times 10^6$ in the convection cell with $\Gamma = 0.5$. It is seen that Nu exhibits two plateaus as marked

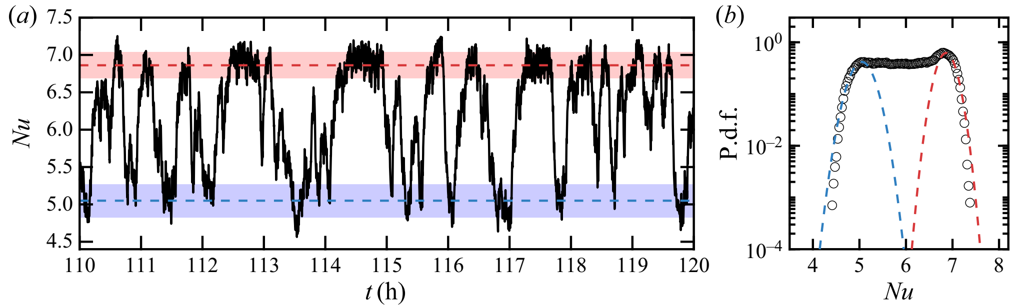

Figure 2. (*a*) A segment of the time series of *Nu* in a 10-day experiment at $Ra = 1.20 \times 10^6$ in the cell with $\Gamma = 0.5$. The upper and lower dashed lines mark $\langle Nu_H \rangle$ and $\langle Nu_L \rangle$, respectively. (*b*) Probability density function (p.d.f.) of *Nu*. The two dashed lines are Gaussian fits to the left tail and the right tail of the p.d.f.

by the two horizontal dashed lines. This bimodal or stepwise transition behaviour of *Nu* can also be seen from its probability density function (p.d.f.) shown in figure 2(*b*). Two broad peaks are apparent in the p.d.f. We fit the left side and the right side of the p.d.f. using Gaussian functions, from which we obtain the mean value of *Nu* and their respective fluctuation characterized by the standard deviation σ_{Nu} for the two states, i.e. $\langle Nu_H \rangle = 6.86$ with $\sigma_{Nu_H} = 0.249$ and $\langle Nu_L \rangle = 5.05$ with $\sigma_{Nu_L} = 0.312$. It is seen that $\langle Nu_H \rangle$ is ∼35 % higher than $\langle Nu_L \rangle$, but the variance of *Nu* of the two states remains almost the same. The observed stepwise transition behaviour of *Nu* suggests that the flow exhibits multiple states with dramatically different heat transport efficiencies.

To understand why the system exhibits multiple heat transport efficiencies, we study the flow structure in the Nu_H state and the Nu_L state. Figure 3(*a*,*b*) shows an example of the time trace of orientation θ and flow strength A of the LSF in the two states. The horizontal axis is normalized by the free-fall time scale τ_{ff}. For $0 < t/\tau_{ff} < 80$, one sees that the dimensionless flow strength $A/\Delta T$ at different z are well above zero and they remain close to each other. Meanwhile, the orientation θ at different z also remains close to each other, which can be seen more clearly in figure 3(*c*) where the time trace of the absolute orientation differences between the top part ($z = 3H/4$), the middle part ($z = H/2$) and the bottom part ($z = H/4$) of the LSF, i.e. $|\delta\theta_{tm}| = 180^\circ - |180^\circ - |\theta_t - \theta_m||$, $|\delta\theta_{mb}| = 180^\circ - |180^\circ - |\theta_b - \theta_m||$ and $|\delta\theta_{bt}| = 180^\circ - |180^\circ - |\theta_b - \theta_t||$, are shown. Note the orientation differences are reduced to the range of $[0, \pi]$ due to the azimuthal symmetry. It is seen that for $0 < t/\tau_{ff} < 80$, the orientation differences are all close to zero. The observation suggests that the LSF is in the form of a planar single-roll structure (also known as the large-scale circulation, LSC) as sketched in figure 3(*e*). For $140 < t/\tau_{ff} < 200$, figure 3(*c*) shows that there is a $\sim\pi/4$ orientation difference between the top part and the middle part, and also between the middle part and the bottom part of the LSF. At the same time, the flow strength A remains well above the widely used threshold of a cessation event (Brown & Ahlers 2006; Xi & Xia 2008; Xie & Xia 2013), i.e. 15 % of the mean flow strength as denoted by the horizontal dash-dotted line in figure 3(*b*), suggesting that the LSF is also well defined during this period of time. Combining the orientation and amplitude behaviour, we conjecture that the LSF is in the form of a twisted single-roll structure, which we named as the twisted LSC as sketched in figure 3(*f*). The corresponding *Nu* of the LSC state and the twisted LSC state is shown in figure 3(*d*) with the two horizontal lines marked Nu_H and Nu_L, respectively. It is seen that the LSC state corresponds to the Nu_H state and the twisted LSC state corresponds to the Nu_L state. One may note that the flow strength at the mid-height of the twisted LSC is smaller compared

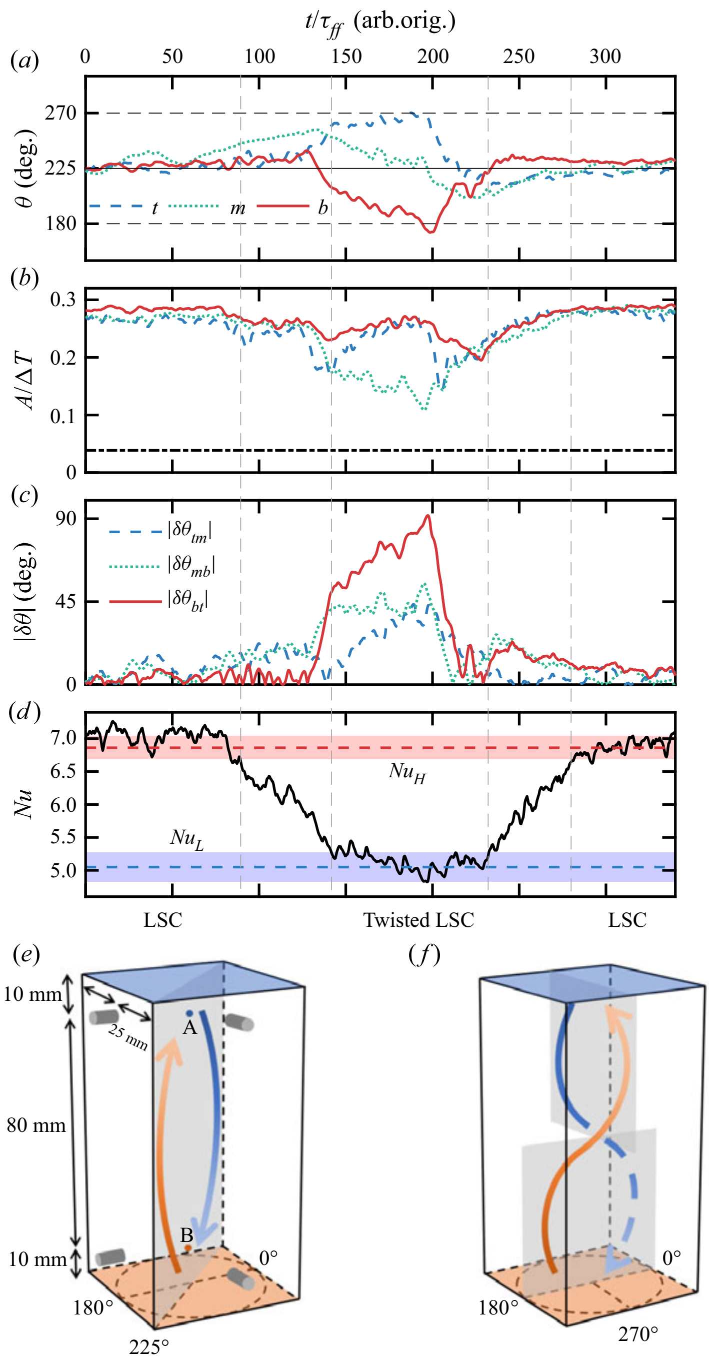

Figure 3. An example showing the transition from the LSC state to the twisted LSC state ($Ra = 1.20 \times 10^6$, $\varGamma = 0.5$). Time trace of (*a*) the orientation θ, (*b*) the flow strength A and (*c*) the absolute value of the orientation difference between the three heights of the large-scale flow. The dash-dotted line in panel (*c*) is 15 % of the average of the maximum flow strength among the three heights, denoting the criterion for a flow cessation. (*d*) Corresponding time trace of Nu. Sketches of (*e*) the LSC state and (*f*) the twisted LSC state. The distributions of the UDV transducers and the velocity measurement points A and B are also depicted in panel (*e*). Vertical dashed lines mark the segment of different flow states.

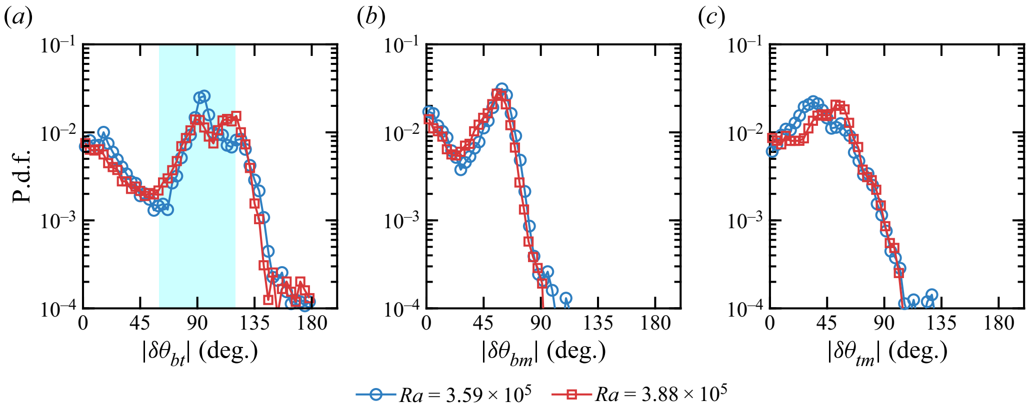

Figure 4. P.d.f.s of the orientation difference between (*a*) the top and bottom heights, (*b*) the bottom and middle heights, and (*c*) the top and middle heights of the large-scale flow measured in the cell of $\Gamma = 0.5$.

with that of the top and bottom heights. A similar observation when the LSF is in the form of a twisted LSC was also reported in a DNS study (Hartmann *et al.* 2021). After going through the twisted LSC state, the orientation at different heights converges and recovers to the LSC state. The transition between two flow states causes a dramatic fluctuation of the Nusselt number.

Schindler *et al.* (2022) reported that the LSC will break down with increasing *Ra* in a cylindrical cell with $\Gamma = 0.5$. They further showed that when the LSC breaks down, coherent flow states (e.g. single-roll or double-roll states) can only last for a few free-fall times. The examples shown in figure 3 suggest that both the LSC state and the twisted LSC state last for several tens of free-fall times. Thus, the large-scale flow is still in a coherent form in the present study. The different dynamics of the LSC observed from the present study and that from Schindler *et al.* (2022) in the $\Gamma = 0.5$ cell may be due to the different range in *Ra*, i.e. the minimum value of *Ra* studied by Schindler *et al.* (2022) ($Ra = 2 \times 10^7$) is larger than the highest *Ra* achieved from the present study. It should also be noted that the different cell geometries, i.e. cuboid cell in the present study and cylindrical cell in the study reported by Schindler *et al.* (2022), could also alter the dynamics of the LSC, as demonstrated by Ji & Brown (2020).

It should be noted that the orientation difference $|\delta\theta_{bt}|$ is not always $\pi/2$ for the twisted state. Figure 4 shows the p.d.f.s of the orientation differences between different heights when the flow is in the twisted-LSC-dominated state. A clear peak located in the range of $[\pi/3, 2\pi/3]$ with its centre at $\pi/2$ is obvious from the p.d.f. of $|\delta\theta_{bt}|$ shown in figure 4(*a*). The broad distribution of $|\delta\theta_{bt}|$ may be caused by the turbulent fluctuations in the system. Meanwhile, the p.d.f.s of $|\delta\theta_{bm}|$ and $|\delta\theta_{tm}|$ show peaks located around $\pi/4$, which is consistent with the twisted structure illustrated in figure 3(*f*). Note a slight asymmetry between the peaks of $|\delta\theta_{bm}|$ and $|\delta\theta_{tm}|$ exists which can result in the asymmetry of the flow structure in the vertical plane.

3.2. *Evolution of the flow state with increasing Ra*

It now becomes clear that the multiple states observed at $Ra = 1.20 \times 10^6$ originate from different structures of the LSF, i.e. a high-*Nu* state with a normal LSC and a low-*Nu* state with a twisted LSC. We next study the Rayleigh number dependence of the observed phenomenon based on the measured *Nu*. Figure 5 shows *Nu* as a function of

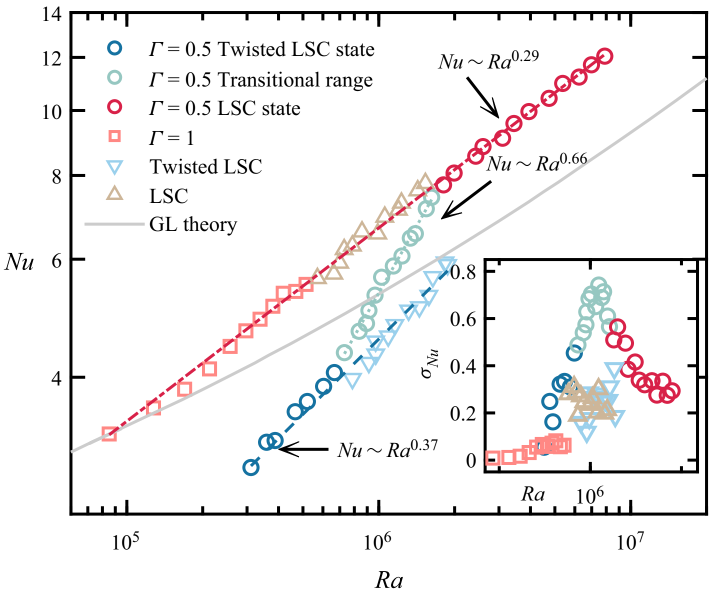

Figure 5. Log-log plot of Nu versus Ra measured in convection cells with $\Gamma = 0.5$ (circles) and $\Gamma = 1$ (squares). The green circles in the $\Gamma = 0.5$ cell stand for the averaged Nu including all data measured for a given Ra in the transitional range, which could be fitted by $Nu = 5 \times 10^{-4} Ra^{0.66}$ (the dotted line). The Nu conditioned on the twisted LSC state and the LSC state in the transitional range are shown as down-pointing triangles and up-pointing triangles, respectively. The dash-dotted line is a power law fit of $Nu = 0.124 Ra^{0.29}$ to the data when the system is in the LSC state. The dashed line is a power law fit of $Nu = 0.026 Ra^{0.37}$ to the data when the system is in the twisted LSC state. The grey solid line denotes the prediction of the Grossmann–Lohse (GL) theory (Grossmann & Lohse 2000; Stevens *et al.* 2013). The inset plots the standard deviation σ_{Nu} of Nu versus Ra for the $\Gamma = 0.5$ and $\Gamma = 1$ cells. The σ_{Nu} of the conditioned LSC state and conditioned twisted LSC state are also shown as up-pointing and down-pointing triangles, respectively.

Ra measured in two convection cells with $\Gamma = 0.5$ and 1. In the cell with $\Gamma = 0.5$, the heat transport scaling, i.e. $Nu \sim Ra^{\alpha}$, shows distinctive regimes characterized by different power laws, i.e. $Nu = 0.026 Ra^{0.37}$ for $3.11 \times 10^5 \leq Ra \leq 6.67 \times 10^5$ (regime I) and $Nu = 0.124 Ra^{0.29}$ for $1.81 \times 10^6 \leq Ra \leq 7.89 \times 10^6$ (regime II). In the transitional range of Ra between the two scaling regimes (referred to as the transitional range hereafter), a $Nu = 5 \times 10^{-4} Ra^{0.66}$ scaling fits the data well, as indicated by the dotted line in the figure. Analysis of the LSF structure shows that the LSF is in the form of the twisted LSC for regime I and it is in the form of the LSC in regime II, which is consistent with the fact that the Nu number of regime II is larger than that of regime I when extrapolating the scaling relation obtained in regime I to regime II. In the transitional range, the data show that the flow switches between the twisted LSC state and the LSC state stochastically, similar to the example shown in figure 2(*a*). As the twisted LSC state and the LSC state show different values of Nu, the switching between the two states results in a dramatic increase in the fluctuation in Nu. The inset of figure 5 shows the root-mean-square value of the Nusselt number σ_{Nu} as a function of Ra. Here σ_{Nu} is defined as $\sigma_{Nu} = \sqrt{\langle (Nu(t) - \langle Nu(t) \rangle)^2 \rangle}$. It is seen that in both regimes I and II, σ_{Nu} remains very small while in the transitional range, σ_{Nu} first increases with Ra, reaches a maximum and then decreases. This increase and decrease of σ_{Nu} signatures the transition of the LSF from the LSC state to the twisted LSC state and *vice versa*. It should be noted that the conditioned standard deviation of Nu, represented by triangles in the inset of figure 5, is of the same order as when the LSF

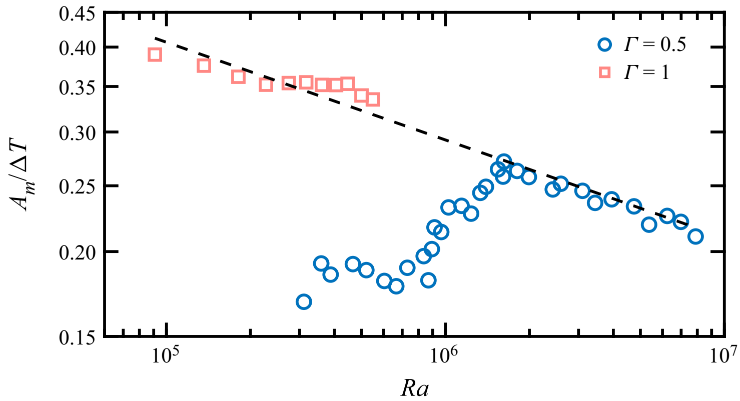

Figure 6. Normalized flow strength $A_m/\Delta T$ at the mid-height versus Ra. The dashed line represents a power law fitting to the data, i.e. $A_m/\Delta T = 2.12 Ra^{-0.14}$.

is in the form of the LSC state or the twisted LSC state. It is also seen from the inset of figure 5 that in the cell with $\Gamma = 1$, σ_{Nu} remains very close to zero, indicating that the LSF is very stable in this configuration. Meanwhile, the corresponding values of Nu in the $\Gamma = 1.0$ cell and that from the $\Gamma = 0.5$ cell at the high Ra number (the flow at the LSC state) can be fitted by a single power law, $Nu = 0.124 Ra^{0.29}$. This power law is in good agreement with existing data at similar Pr (Naert, Segawa & Sano 1997; Glazier *et al.* 1999; Zürner *et al.* 2019; Schindler *et al.* 2022). The solid line in figure 5 is a plot of the prediction from the Grossmann–Lohse theory (Grossmann & Lohse 2000) with updated parameters obtained from cylindrical cells (Stevens *et al.* 2013). It is seen that the theory underestimates Nu. A possible reason may be due to the difference in cell geometry.

Detailed examination of the flow structure using the temperature profiles measured inside the sidewall shows that the LSF is in the LSC state in the cell with $\Gamma = 1$. This can be seen clearly from figure 6, where we plot the normalized flow strength A_m of the LSF measured at the mid-height of the cell. It is seen that in the cell with $\Gamma = 1$, $A_m/\Delta T$ decreases with Ra. In the cell with $\Gamma = 0.5$, however, $A_m/\Delta T$ first increases with Ra and starts to decrease with Ra for $Ra > 1.62 \times 10^6$. The transitional Ra of $A_m/\Delta T$ is similar to the transitional Ra observed from the Nusselt number measurements shown in figure 5, suggesting that the transition of the flow state occurs concurrently with the transition of the heat transport efficiency. Note, in both cells, the decrease of $A_m/\Delta T$ with Ra can be fitted by a single power law, i.e. $A_m/\Delta T \sim Ra^{-0.14}$. This can be regarded as consistent with the observed unified power law relation between Nu and Ra for the LSC state shown in figure 5.

3.3. *Flow dynamics in the transitional range*

The switching between the LSC state and the twisted LSC state is a distinct feature of the transitional range. To further understand the dynamics of this switching, we study the time percentage of the the LSC state and the twisted LSC state, and the time interval between them. The following algorithm was used to identify different flow states based on the time series of $Nu(t)$. If $Nu(t) > Nu_H - \sigma_{Nu_H}$, the flow is classified as the LSC state. If $Nu(t) < Nu_L + \sigma_{Nu_L}$, the flow is classified as the twisted LSC state (see red and blue shadows in figure 2*a*). The rest of the time is classified as the transitional state.

Figure 7 shows the time percentage w when the flow stays in different states. It is seen that at the low end of Ra, the flow is dominated by the twisted LSC state. With increasing

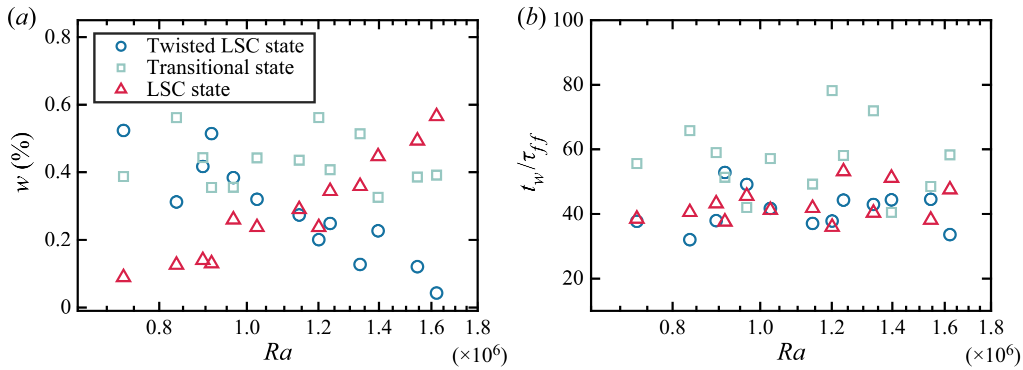

Figure 7. (*a*) The time percentage of the flow stays at the twisted LSC state, transitional state and the LSC state in the transitional range. (*b*) Normalized mean lifetime of the three states in the transitional range.

Ra, the time percentage w of the LSC state gradually increases and becomes dominant for the highest *Ra* in the transitional range. Meanwhile, the time percentage w of the twisted LSC state decreases with increasing *Ra* and becomes close to zero at the highest *Ra* in the transitional range. The time percentage w of the transitional state depends weakly on *Ra* as revealed by the squares in figure 7(*a*). Figure 7(*b*) plots the normalized mean lifetime t_w/τ_{ff} of the three states. Despite the data being of scatter, one sees that t_w/τ_{ff} seems to be independent of *Ra* with a mean value of $\sim 60\tau_{ff}$ for the transitional state, and $\sim 40\tau_{ff}$ for the twisted LSC state and the LSC state.

The observed twisted LSC state reminds one of the twisting oscillation of the planar LSC observed in turbulent RBC (Xi *et al.* 2009; Weiss & Ahlers 2011; Zwirner *et al.* 2020*a*). However, the twisted LSC state observed in the present study is different from the twisting oscillation in terms of their time scale. For example, at $Ra = 1.42 \times 10^7$, the twisting oscillation period reported by Zwirner *et al.* (2020*a*) is $\sim 9.2\tau_{ff} \approx 12s$. The LSC turn-over time estimated based on the velocity measurement reported by Khalilov *et al.* (2018) is $\tau_{LSC} = (4H)/(v_{LSC}) = 4 \times 0.216/0.063s \approx 14s$. One sees that the twisting oscillation is of the same time scale as the LSC turn-over time ($\sim 0.9\tau_{LSC}$). In the present study, the twisted LSC state lasted approximately $40\tau_{ff}$ at $Ra = 1.20 \times 10^6$. The LSC turn-over time estimated from the direct velocity measurement performed using ultrasonic Doppler velocimetry is $\tau_{LSC} = (2D + 2H)/(v_{LSC}) = (2 \times 0.05 + 2 \times 0.103)/0.004s \approx 76s$, which is approximately $14.5\tau_{ff}$. Thus, the twisted LSC lasted approximately $3\tau_{LSC}$. The difference between the time scale of the twisted LSC and that of the twisting oscillation suggests that they have different flow dynamics occurring on different time scales. Thus the twisted LSC and the twisting oscillation of the LSC are two different natures of the LSF in liquid metal convection. It is worthy mentioning that, unlike the periodic motion of the twisting oscillation, the occurrence of the twisted LSC state is not periodic. One should notice that the twisted LSC state is a flow structure, which is different from the dynamical switching of the LSC plane between different body diagonals of a cubic cell, such as those reported by Ji & Brown (2020).

3.4. *Temperature fluctuation at the cell centre for different flow states*

To further shed light upon the difference between flow states in cells with $\Gamma = 0.5$ and $\Gamma = 1$ when *Ra* is the same, we study the temperature fluctuations at the cell centre. Figures 8(*a*) and 8(*b*) plot the time trace of the normalized temperature fluctuation

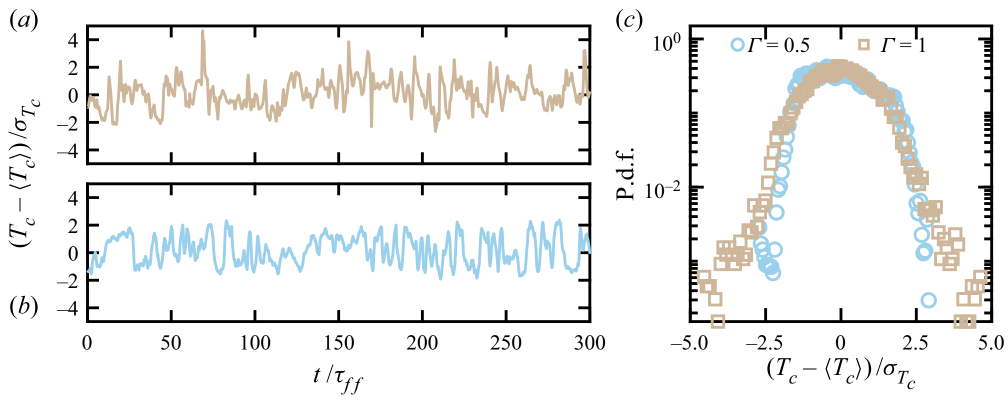

Figure 8. Time series of normalized temperature fluctuations measured in the centre of (*a*) the $\Gamma = 1$ and (*b*) the $\Gamma = 0.5$ cell at $Ra = 5 \times 10^5$. (*c*) P.d.f. of the standardized temperature fluctuation at the cell centre.

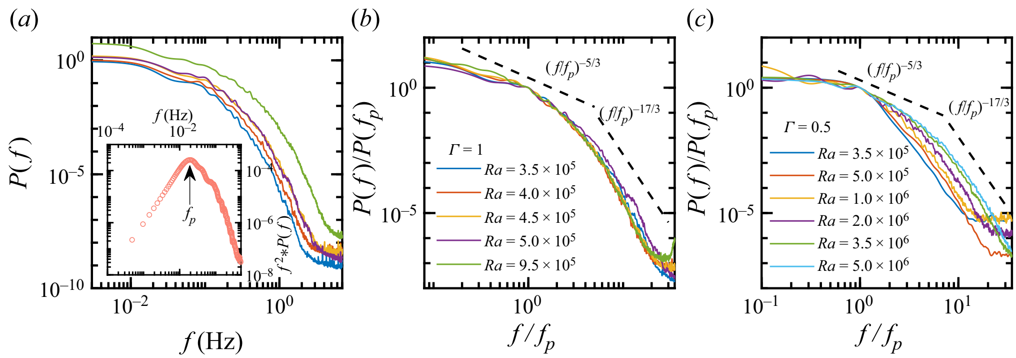

Figure 9. (*a*) Original temperature PSD at the cell centre for the same *Ra* of panel (*b*) in the $\Gamma = 1$ cell. The inset shows the temperature dissipation spectrum and its peak value f_p. The scaled temperature power spectrum density (PSD) for various *Ra* in the cell with (*b*) $\Gamma = 1$ and (*c*) $\Gamma = 0.5$. The dashed lines in panel (*b*,*c*) indicate two scaling regimes, i.e. inertial-convective subrange with $P(f) \sim f^{-5/3}$ and inertial-conductive subrange with $P(f) \sim f^{-17/3}$.

$(T_c - \langle T_c \rangle)/\sigma_{T_c}$ at $Ra = 5 \times 10^5$ for cells with $\Gamma = 1$ and $\Gamma = 0.5$, respectively. From the heat transport data shown in figure 5, one knows that the LSF is in the form of the normal LSC state in the $\Gamma = 1$ cell and it is in the form of the twisted LSC state in the $\Gamma = 0.5$ cell. It is seen that there exist sharp spikes in the time trace of the temperature fluctuation in the $\Gamma = 1$ cell, which could be conjectured as signatures of thermal plumes (Shang *et al.* 2004). However, the temperature fluctuation time trace shows that temperature fluctuation is confined between $\langle T \rangle \pm 2.5\sigma_T$ in the $\Gamma = 0.5$ cell. The difference in the nature of temperature fluctuation can be seen more clearly from their respective p.d.f.s shown in figure 8(*c*). It is seen that the largest temperature fluctuations can reach almost $\langle T \rangle \pm 5\sigma_T$ in the $\Gamma = 1$ cell. However, it only reaches $\langle T \rangle \pm 2.5\sigma_T$ in the $\Gamma = 0.5$ cell.

To quantify the difference in the temporal dynamics of the temperature fluctuation. We study their power spectra density (PSD). Figures 9(*b*) and 9(*c*) show the PSD of T_c measured in cells with $\Gamma = 1.0$ and $\Gamma = 0.5$, respectively. To compare the PSD from different *Ra*, the frequency axis is normalized by the peak frequency f_p obtained from the dissipation spectra, i.e. $f^2P(f)$ versus f (She & Jackson 1993; Zhou & Xia 2001). Here, $f^2P(f)$ is calculated based on the original PSD of the temperature at the cell centre shown in figure 9(a). The dissipation PSD is shown in the inset of figure 9(a). In figures 9(b) and 9(c), the vertical axis is normalized by the value of the PSD corresponding to f_p. It is seen from figure 9(b) that the normalized PSD in the cell with $\varGamma = 1$ for different values of Ra show a universal shape. In addition, the PSDs in the $\varGamma = 1$ cell show two scaling regimes characterized by $P(f)/P(f_p) \sim (f/f_p)^{-5/3}$ and $P(f)/P(f_p) \sim (f/f_p)^{-17/3}$. The appearance of the two scaling regimes indicates that the flow in the studied parameter range is in the form of developed turbulence (Batchelor, Howells & Townsend 1959). This is consistent with the recent study reporting that the flow will be turbulent when $Ra > 1.0 \times 10^5$ in liquid metal convection with $\varGamma = 1$ (Ren *et al.* 2022). The PSDs measured in the cell with $\varGamma = 0.5$ show different behaviours. It is seen from figure 9(c) that the shape of the normalized PSDs changes with increasing Ra. For $Ra < 5.0 \times 10^5$, the PSDs show no evidence of developed turbulence. When $Ra > 3.5 \times 10^6$, the PSDs show two scaling regimes similar to the cell with $\varGamma = 1$. The observation suggests that in the cell with $\varGamma = 0.5$, when Ra is increased from the lowest end of the studied parameter range, the flow gradually evolves to the fully developed turbulence state with a single roll LSC for $Ra > 1.80 \times 10^6$.

The change in the shape of the PSDs in the $\varGamma = 0.5$ cell and the Ra-dependence of the flow strength can be regarded as being consistent with the heat transport data shown in figure 5. When $Ra < 1.80 \times 10^6$, the bulk flow is in the turbulence state in the cell with $\varGamma = 1$. However, the flow is in the regime before the transition to fully developed turbulence in the cell with $\varGamma = 0.5$. This difference in the bulk flow state could possibly originate from the strength of the LSF. As it is seen from figure 6, the flow strength of the LSC is larger than that of the twisted LSC. The turbulence at the cell centre gains energy from the shear produced by the LSF (Xia, Sun & Zhou 2003). A stronger LSC will result in a more turbulent flow. In addition, there exists bistability when the system gradually evolves towards fully developed turbulence in the cell with $\varGamma = 0.5$. The PSDs continuously evolve with Ra and show two slopes when $Ra > 2 \times 10^6$, implying that the flow will become fully developed for $Ra > 2 \times 10^6$.

4. Conclusion

We show experimentally that the heat transport in low-Prandtl-number thermal convection can show intriguing dependence on the flow structures. In a cell with $\varGamma = 0.5$, the large-scale flow exhibits two states: a twisted LSC state with its heat transport efficiency being $\sim$35 % smaller than a normal LSC state. The twisted LSC state differs from the twisting oscillation in terms of its time scale. With increasing the level of turbulence, the system gradually evolves from the twisted LSC state with $Nu \sim Ra^{0.37}$ to the LSC state with $Nu \sim Ra^{0.29}$. Bistability is observed before the system becomes fully developed turbulence for $Ra > 1.80 \times 10^6$. Combining measurements in cells with $\varGamma = 1$ and 0.5, the study shows that the large-scale flow exhibits a self-similar LSC structure when the system is in the fully developed turbulence state, characterized by a universal power law for the heat transport, i.e. $Nu \sim Ra^{0.29}$. The study demonstrates experimentally that a strong coupling between the large-scale flow and heat transport exits in low-Pr-number thermal convection, which makes it possible to control heat transport via tuning of the large-scale flow in convection.

Funding. This work is supported by National Natural Science Foundation (NSFC) under grant numbers 51927812, 92152104, 52176086, 12002260 and 52222607, the National Key R&D Program of China under grant number 2022YFE03130000 and Fundamental Research Funds for the Central Universities (xzy012021005).

Declaration of interests. The authors report no conflict of interest.

Author ORCIDs.
Xin-Yuan Chen https://orcid.org/0000-0002-8521-7334;
Yi-Chao Xie https://orcid.org/0000-0002-2159-4579;
Juan-Cheng Yang https://orcid.org/0000-0002-5834-5680;
Ming-Jiu Ni https://orcid.org/0000-0003-3699-8370.

Author contributions. X.-Y. Chen and Y.-C. Xie contributed equally to this work.

References

Ahlers, G., Grossmann, S. & Lohse, D. 2009 Heat transfer and large scale dynamics in turbulent Rayleigh-Bénard convection. *Rev. Mod. Phys.* **81** (2), 503.

Aurnou, J.M., Bertin, V., Grannan, A.M., Horn, S. & Vogt, T. 2018 Rotating thermal convection in liquid gallium: multi-modal flow, absent steady columns. *J. Fluid Mech.* **846**, 846–876.

Aurnou, J.M. & Olson, P.L. 2001 Experiments on Rayleigh–Bénard convection, magnetoconvection and rotating magnetoconvection in liquid gallium. *J. Fluid Mech.* **430**, 283–307.

Batchelor, G.K., Howells, I.D. & Townsend, A.A. 1959 Small-scale variation of convected quantities like temperature in turbulent fluid part 2. The case of large conductivity. *J. Fluid Mech.* **5** (1), 134–139.

Brown, E. & Ahlers, G. 2006 Rotations and cessations of the large-scale circulation in turbulent Rayleigh–Bénard convection. *J. Fluid Mech.* **568**, 351–386.

Brown, E. & Ahlers, G. 2009 The origin of oscillations of the large-scale circulation of turbulent Rayleigh–Bénard convection. *J. Fluid Mech.* **638**, 383–400.

Cioni, S., Ciliberto, S. & Sommeria, J. 1997 Strongly turbulent Rayleigh–Bénard convection in mercury: comparison with results at moderate Prandtl number. *J. Fluid Mech.* **335**, 111–140.

Cortet, P., Chiffaudel, A., Daviaud, F. & Dubrulle, B. 2010 Experimental evidence of a phase transition in a closed turbulent flow. *Phys. Rev. Lett.* **105** (21), 214501.

Elsasser, W.M. 1956 Hydromagnetic dynamo theory. *Rev. Mod. Phys.* **28** (2), 135.

Faranda, D., Sato, Y., Saint-Michel, B., Wiertel, C., Padilla, V., Dubrulle, B. & Daviaud, F. 2017 Stochastic chaos in a turbulent swirling flow. *Phys. Rev. Lett.* **119** (1), 014502.

Glazier, J.A, Segawa, T., Naert, A. & Sano, M. 1999 Evidence against 'ultrahard' thermal turbulence at very high Rayleigh numbers. *Nature* **398** (6725), 307–310.

Grooms, I., Julien, K., Weiss, J.B. & Knobloch, E. 2010 Model of convective Taylor columns in rotating Rayleigh-Bénard convection. *Phys. Rev. Lett.* **104** (22), 224501.

Grossmann, S. & Lohse, D. 2000 Scaling in thermal convection: a unifying theory. *J. Fluid Mech.* **407**, 27–56.

Hartmann, R., Chong, K.L., Stevens, R.J.A.M., Verzicco, R. & Lohse, D. 2021 Heat transport enhancement in confined Rayleigh-Bénard convection feels the shape of the container. *Europhys. Lett.* **135** (2), 24004.

Huisman, S.G., Van Der Veen, R.C., Sun, C. & Lohse, D. 2014 Multiple states in highly turbulent Taylor–Couette flow. *Nat. Commun.* **5** (1), 1–5.

Ji, D. & Brown, E. 2020 Low-dimensional model of the large-scale circulation of turbulent Rayleigh-Bénard convection in a cubic container. *Phys. Rev.* E **5** (6), 064606.

Khalilov, R., Kolesnichenko, I., Pavlinov, A., Mamykin, A., Shestakov, A. & Frick, P. 2018 Thermal convection of liquid sodium in inclined cylinders. *Phys. Rev. Fluids* **3** (4), 043503.

King, E.M. & Aurnou, J.M. 2013 Turbulent convection in liquid metal with and without rotation. *Proc. Natl Acad. Sci.* **110** (17), 6688–6693.

Lohse, D. & Xia, K.-Q. 2010 Small-scale properties of turbulent Rayleigh-Bénard convection. *Annu. Rev. Fluid Mech.* **42**, 335–364.

Naert, A., Segawa, T. & Sano, M. 1997 High-Reynolds-number thermal turbulence in mercury. *Phys. Rev.* E **56** (2), R1302.

Plevachuk, Y., Sklyarchuk, V., Eckert, S., Gerbeth, G. & Novakovic, R. 2014 Thermophysical properties of the liquid Ga–In–Sn eutectic alloy. *J. Chem. Engng Data* **59** (3), 757–763.

Ravelet, F., Marié, L., Chiffaudel, A. & Daviaud, F. 2004 Multistability and memory effect in a highly turbulent flow: experimental evidence for a global bifurcation. *Phys. Rev. Lett.* **93** (16), 164501.

Ren, L., Tao, X., Zhang, L., Ni, M.-J., Xia, K.-Q. & Xie, Y.-C. 2022 Flow states and heat transport in liquid metal convection. *J. Fluid Mech.* **951**, R1.

Salavy, J., Boccaccini, L.V., Lässer, R., Meyder, R., Neuberger, H., Poitevin, Y., Rampal, G., Rigal, E., Zmitko, M. & Aiello, A. 2007 Overview of the last progresses for the European test blanket modules projects. *Fusion Engng Des.* **82** (15-24), 2105–2112.

Schindler, F., Eckert, S., Zürner, T., Schumacher, J. & Vogt, T. 2022 Collapse of coherent large scale flow in strongly turbulent liquid metal convection. *Phys. Rev. Lett.* **128** (16), 164501.

Shang, X.-D., Qiu, X.-L., Tong, P. & Xia, K.-Q. 2004 Measurements of the local convective heat flux in turbulent Rayleigh-Bénard convection. *Phys. Rev.* E **70** (2), 026308.

She, Z.-S. & Jackson, E. 1993 On the universal form of energy spectra in fully developed turbulence. *Phys. Fluids* **5** (7), 1526–1528.

Stevens, R.J.A.M., van der Poel, E.P., Grossmann, S. & Lohse, D. 2013 The unifying theory of scaling in thermal convection: the updated prefactors. *J. Fluid Mech.* **730**, 295–308.

Sun, C., Xi, H.-D. & Xia, K.-Q. 2005 Azimuthal symmetry, flow dynamics, and heat transport in turbulent thermal convection in a cylinder with an aspect ratio of 0.5. *Phys. Rev. Lett.* **95** (7), 074502.

de la Torre, A. & Burguete, J. 2007 Slow dynamics in a turbulent von Kármán swirling flow. *Phys. Rev. Lett.* **99** (5), 054101.

Verzicco, R. & Camussi, R. 2003 Numerical experiments on strongly turbulent thermal convection in a slender cylindrical cell. *J. Fluid Mech.* **477**, 19–49.

Wang, Q., Verzicco, R., Lohse, D. & Shishkina, O. 2020 Multiple states in turbulent large-aspect-ratio thermal convection: what determines the number of convection rolls? *Phys. Rev. Lett.* **125** (7), 074501.

Weiss, S. & Ahlers, G. 2011 Turbulent Rayleigh–Bénard convection in a cylindrical container with aspect ratio $\gamma = 0.50$ and Prandtl number $Pr = 4.38$. *J. Fluid Mech.* **676**, 5–40.

de Wit, X.M., van Kan, A. & Alexakis, A. 2022 Bistability of the large-scale dynamics in quasi-two-dimensional turbulence. *J. Fluid Mech.* **939**, R2.

Xi, H.-D. & Xia, K.-Q. 2008 Flow mode transitions in turbulent thermal convection. *Phys. Fluids* **20** (5), 055104.

Xi, H.-D., Zhou, S.-Q., Zhou, Q., Chan, T.-S. & Xia, K.-Q. 2009 Origin of the temperature oscillation in turbulent thermal convection. *Phys. Rev. Lett.* **102** (4), 044503.

Xia, K.-Q. 2013 Current trends and future directions in turbulent thermal convection. *Theor. Appl. Mech. Lett.* **3** (5), 052001.

Xia, K.-Q., Sun, C. & Zhou, S.-Q. 2003 Particle image velocimetry measurement of the velocity field in turbulent thermal convection. *Phys. Rev.* E **68** (6), 066303.

Xie, Y.-C., Ding, G.-Y. & Xia, K.-Q. 2018 Flow topology transition via global bifurcation in thermally driven turbulence. *Phys. Rev. Lett.* **120** (21), 214501.

Xie, Y.-C., Wei, P. & Xia, K.-Q. 2013 Dynamics of the large-scale circulation in high-Prandtl-number turbulent thermal convection. *J. Fluid Mech.* **717**, 322–346.

Xie, Y.-C. & Xia, K.-Q. 2013 Dynamics and flow coupling in two-layer turbulent thermal convection. *J. Fluid Mech.* **728**, R1.

Xu, Y., Horn, S. & Aurnou, J.M. 2022 Thermoelectric precession in turbulent magnetoconvection. *J. Fluid Mech.* **930**, A8.

Yanagisawa, T., Yamagishi, Y., Hamano, Y., Tasaka, Y. & Takeda, Y. 2011 Spontaneous flow reversals in Rayleigh-Bénard convection of a liquid metal. *Phys. Rev.* E **83** (3), 036307.

Yanagisawa, T., Yamagishi, Y., Hamano, Y., Tasaka, Y., Yoshida, M., Yano, K. & Takeda, Y. 2010 Structure of large-scale flows and their oscillation in the thermal convection of liquid gallium. *Phys. Rev.* E **82** (1), 016320.

Yang, Y., Chen, W., Verzicco, R. & Lohse, D. 2020 Multiple states and transport properties of double-diffusive convection turbulence. *Proc. Natl Acad. Sci.* **117** (26), 14676–14681.

Yang, J.C., Vogt, T. & Eckert, S. 2021 Transition from steady to oscillating convection rolls in Rayleigh-Bénard convection under the influence of a horizontal magnetic field. *Phys. Rev. Fluids* **6**, 023502.

Zhou, S.-Q. & Xia, K.-Q. 2001 Scaling properties of the temperature field in convective turbulence. *Phys. Rev. Lett.* **87** (6), 064501.

Zimmerman, D.S., Triana, S.A. & Lathrop, D.P. 2011 Bi-stability in turbulent, rotating spherical Couette flow. *Phys. Fluids* **23** (6), 065104.

Zürner, T., Schindler, F., Vogt, T., Eckert, S. & Schumacher, J. 2019 Combined measurement of velocity and temperature in liquid metal convection. *J. Fluid Mech.* **876**, 1108–1128.

Zwirner, L., Khalilov, R., Kolesnichenko, I., Mamykin, A., Mandrykin, S., Pavlinov, A., Shestakov, A., Teimurazov, A., Frick, P. & Shishkina, O. 2020*a* The influence of the cell inclination on the heat transport and large-scale circulation in liquid metal convection. *J. Fluid Mech.* **884**, A18.

Zwirner, L., Tilgner, A. & Shishkina, O. 2020*b* Elliptical instability and multiple-roll flow modes of the large-scale circulation in confined turbulent Rayleigh-Bénard convection. *Phys. Rev. Lett.* **125** (5), 054502.